Hypersonic Flow over a Blunt Body with Finite Difference Method and Equilibrium Real Gas Model

Yung-Tien Lin*
University of California, Los Angeles, California, 90095

This research project aims to develop a computational fluid dynamics (CFD) program for simulating hypersonic flow over a blunt body (up to Mach 30) with a chemical equilibrium gas model. The goal of the project is to capture the real gas effect of the hypersonic flow and study the influence of the effect on temperature distributions. The fluid flow is assumed inviscid and described by the two-dimensional Euler equations. For the real gas model, the proposed gas model consists of eight species ($N_2, O_2, NO, N, O, N^+, O^+$, and e^-) and uses five chemical equilibrium equations to simulate the chemical dissociation at equilibrium states. The first-order upwind finite difference method is used for the spatial discretization and flux splitting is done by the local Lax-Friedrich method. To ensure the species composition converged during the real gas simulation, this project used a precomputed interpolation table to generate the initial guess of the gas composition. Finally, the resulting 8-species gas model is verified and the values are consistent with the literature. The CFD simulation also reproduced the results from the equilibrium normal shock relation and captured the bow shock physics qualitatively.

I. Nomenclature

A, B	=	arbitrary constants for calculations
c	=	mass fraction
c_v	=	heat capacity
e	=	internal energy per unit mass
E	=	total energy per unit volume
$\vec{E}, \vec{F}$	=	state fluxes in x and y direction respectively
g	=	degeneracy
h	=	Planck constant
k	=	Boltzmann constant
K_p	=	Equilibrium constant for partial pressures
m	=	mass per particle
$\hat{M}$	=	mass per mole
N	=	mole number
p	=	pressure
Q	=	partition function
R	=	gas constant for species/mixture
$\hat{R}$	=	universal gas constant
s	=	entropy per unit mass
T	=	temperature
$\vec{U}$	=	state vector
V	=	volume
γ	=	heat capacity ratio
η	=	mole number per unit mixture mass
ν	=	stoichiometric number
Θ	=	characteristic temperature
ρ	=	density
σ	=	hetero/homonuclear number

*Ph.D. Student, Mechanical and Aerospace Engineering, yungtlin@g.ucla.edu, AIAA Student Member.

Superscripts and Subscripts

$e^s, Q^s, \ldots$	=	species
$c_s, \rho_s, \eta_s, \ldots$	=	species
R_0, γ_0	=	ideal condition
$Q_{el}, e_{el}, s_{el}, \ldots$	=	electronic mode
$Q_{rot}, e_{rot}, s_{rot}, \ldots$	=	rotational mode
$Q_{trans}, e_{trans}, s_{trans}, \ldots$	=	translational mode
$Q_{vib}, e_{vib}, s_{vib}, \ldots$	=	vibrational mode
$g_0, g_1, \Theta_1, \ldots$	=	degeneracy mode

II. Introduction

Hypersonic research has become one of the critical fields for defense technology development [1]. However, high-temperature aerodynamics posed challenges to engineers and researchers in studying the physics of the hypersonic flow. For example, the experimental study of hypersonic aerodynamics required a sophisticated heat tank to store high-enthalpy gas for replicating the cruising conditions. Therefore, another approach to work on the hypersonic flow is using CFD simulation. However, unlike other lower-speed flows, hypersonic requires additional chemical models to predict fluid dissociation under high temperatures. Therefore a study of high-temperature thermodynamics is necessary for the hypersonic flow study. As a result, this project works on building an equilibrium model to simulate the high-temperature behaviors. Even though for the high Mach number, the flow tends to be non-equilibrium due to the extremely small flow time. This equilibrium assumption is still valid for the primitive study of hypersonic flow physics.

III. Real Gas Model

A. Equilibrium Model for Air

For the hypersonic simulation, a real gas model is necessary for simulating gas dissociation and capturing thermodynamic properties under high temperatures. Otherwise, an ideal calorically perfect gas will significantly over-predict the temperature and result in unrealistic data for high Mach numbers. The project uses air as the working gas and assumes air will dissociate into eight species, which are N_2, O_2, NO, N, O, N^+, O^+, and e^-, for temperature range from 300K to 16, 000K and pressure range from 10^{-4} to 10^2 atm. The initial gas composition for nitrogen and oxygen is based on the ratio at sea level. Other gas species, such as CO_2 and Ar, are discarded due to the low mass composition in the air and stable chemical properties of the inert gas. Then chemical dissociation and ionization physics are governed by the five chemical equilibrium equations which are:

$$\begin{aligned} N_2 &\leftrightarrow 2N \\ O_2 &\leftrightarrow 2O \\ NO &\leftrightarrow N + O \\ N &\leftrightarrow N^+ + e^- \\ O &\leftrightarrow O^+ + e^- \end{aligned} \tag{1}$$

For the thermodynamic properties of the species under high temperatures, this project uses the four energy modes to estimate the species' behaviors. The estimation of those properties will also be used for computing the chemical equilibrium constants for dissociation and ionization. In the following sections, the ideal gas model refers to the calorically perfect gas and the real gas model means the eight-species equilibrium model presented in here.

B. Energy Modes

The high-temperature thermodynamics can be evaluated through the four energy modes of molecules. The four energy modes are, based on the type of motion, translational, rotational, vibrational, and electronic modes. The translational and electronic modes are universal for both monatomic and diatomic species. The rotational and vibrational modes are specific to diatomic species because the modes are related to intermolecular motion. Each mode has its functions and the production and summation of each mode's thermodynamic properties form the overall behaviors of

the species. The following paragraph describes the analytical form of the modes and will be used for the real gas model computation of the later sections.

Translational mode refers to the motion of the translational movement of the molecule. This is also the only mode considered an external mode since it directly interacts with the volume of a given space. The partition function, internal energy, constant volume heat capacity, and entropy of the mode are given as followed:

$$\begin{aligned} Q_{trans} &= V\left[\frac{2\pi mkT}{h^2}\right]^{3/2} \\ e_{trans} &= \frac{3}{2}RT \\ c_{v,trans} &= \frac{3}{2}R \\ s_{trans} &= \frac{5}{2}R\ln(T) - R\ln p + R\left\{\ln\left[\left(\frac{2\pi m}{h^2}\right)^{3/2}k^{5/2}\right] + \frac{5}{2}\right\} \end{aligned} \tag{2}$$

The rotational mode is the spinning motion about the molecule center. In addition to the other modes, the rotational mode needs to consider the symmetry of the molecule structure due to the moment of inertia. The hetero/homonuclear number, σ, is used for taking the symmetry into account. For asymmetric or heteronuclear species, such as NO, the hetero/homonuclear number is 1 and the number becomes 2 for homonuclear species. For most of the scenarios, especially for high-temperature conditions, the rotational mode is fully excited and the internal energy is linearly related to the temperature. The thermodynamic properties of the rotational mode are given as follows:

$$\begin{aligned} Q_{rot} &= \frac{T}{\sigma\Theta_r} \\ e_{rot} &= RT \\ c_{v,rot} &= R \\ s_{rot} &= R\left[\ln\frac{T}{\sigma\Theta_r} + 1\right] \end{aligned} \tag{3}$$

The vibrational mode describes the contraction/relaxation motion of the atoms inside the molecule. This mode most of the time remains inactive or negligible for lower temperatures. For temperature around the vibrational characteristic temperature Θ_v, the mode becomes significant and will be fully excited at higher temperatures. The thermodynamic properties of the vibrational mode are given as follows:

$$\begin{aligned} Q_{vib} &= \frac{1}{1 - e^{-\Theta_v/T}} \\ e_{vib} &= \frac{R\Theta_v}{e^{\Theta_v T} - 1} \\ c_{v,vib} &= R\left[\frac{\Theta_v/(2T)}{\sinh\left(\Theta_v/2T\right)}\right]^2 \\ s_{vib} &= R\left[-\ln\left(1 - e^{-\Theta_v/T}\right)\right] \end{aligned} \tag{4}$$

The electronic mode is the kinematic motion from the electron orbiting the nucleus. The thermodynamic properties of the electronic mode are evaluated through the degeneracy levels with two-term approximation:

$$\begin{aligned} Q_{el} &= g_0 + g_1 e^{-\Theta_1/T} \\ e_{el} &= R\Theta_1\frac{(g_1/g_0)e^{-\Theta_1/T}}{1 + (g_1/g_0)e^{-\Theta_1/T}} \\ c_{v,el} &= R\left(\frac{\Theta_1}{T}\right)^2\frac{(g_1/g_0)e^{-\Theta_1/T}}{\left[1 + (g_1/g_0)e^{-\Theta_1/T}\right]^2} \\ s_{el} &= R\left[\ln(g_0) + \ln\left(1 + \frac{g_1}{g_0}e^{-\Theta_1/T}\right) + \frac{(g_1/g_0)(\Theta_1/T)e^{-\Theta_1/T}}{\left[1 + (g_1/g_0)e^{-\Theta_1/T}\right]^2}\right] \end{aligned} \tag{5}$$

Finally, the zero energy convention of this project is based on the stablest species under room temperature which are N_2 and O_2. This convention prevents having a negative zero energy for other species. The zero energy for each species is computed as follows:

$$e_0 = R\Theta_z \tag{6}$$

Table 1 Physical properties for the species

Species	$\hat{M}$	Θ_z	g_0	g_1	Θ_1	Θ_r	σ	Θ_v
N_2	28×10^{-3}	0	1	0	0	2.9	2	3,390
O_2	32×10^{-3}	0	3	2	11,390	2.1	2	2,270
NO	30×10^{-3}	10,750	2	2	174	2.5	1	2,740
N	14×10^{-3}	56,500	4	10	27,700			
O	16×10^{-3}	29,750	5	4	270			
N^+	14×10^{-3}	225,500	1	8	145			
O^+	16×10^{-3}	187,750	4	10	38,600			
e^-	5.486×10^{-7}	0	2	0	0			

Table 1 shows the required physical properties of each species to compute the modes. With those values, one may estimate the thermodynamic properties under high temperatures and the chemical equilibrium constant for dissociation can be evaluated.

C. Law of Mass Action

The general form of the chemical reaction can be expressed as follows:

$$|\nu_a|a \leftrightarrow |\nu_b|b + |\nu_c|c \tag{7}$$

where the sign of the stoichiometric number, ν, for reactants is positive and for products is negative. The partial pressure for each species at the equilibrium states can be estimated from the law of mass action:

$$K_p = \prod_s {p_s}^{\nu_s} \tag{8}$$

The equilibrium constants for partial pressure can be estimated from the statistical mechanics:

$$K_p = \left(\frac{1}{kT}\right)^{\sum_s \nu_s} \prod_s \left(f_{trans} \prod_{int} Q^s_{int} \right)^{-\nu_s} e^{-D/kT} \tag{9}$$

where the f is the translational partition function over a given volume:

$$Q_{trans}(V,T) = V \left[\frac{2\pi mkT}{h^2}\right]^{3/2} = V f_{trans}(T) \tag{10}$$

With the equilibrium constants, the model can start formulating the constraints for the partial pressures and estimating the species composition at the equilibrium states.

D. Constraints for the Equilibrium Model

If the pressure and temperature are given, the eight-species model requires eight constraints to establish a closed-form solution. With the above relation of partial pressure, the eight partial pressures satisfy the following eight constraints: The dissociation of $N_2 \leftrightarrow 2N$:

$$\frac{(p_N)^2}{p_{N_2}} = K_{p,1}(T) \tag{11}$$

The dissociation of $O_2 \leftrightarrow 2O$:

$$\frac{(p_O)^2}{p_{O_2}} = K_{p,2}(T) \tag{12}$$

The dissociation of $NO \leftrightarrow N + O$:

$$\frac{p_N p_O}{p_{NO}} = K_{p,3}(T) \tag{13}$$

The ionization of $N \leftrightarrow N^+ + e^-$:

$$\frac{p_{N^+} p_{e^-}}{p_N} = K_{p,4}(T) \tag{14}$$

The ionization of $O \leftrightarrow O^+ + e^-$:

$$\frac{p_{O^+} p_{e^-}}{p_O} = K_{p,5}(T) \tag{15}$$

The conservation of atoms:

$$\frac{2p_{N_2} + p_{NO} + p_N + p_{N^+}}{2p_{O_2} + p_{NO} + p_O + p_{O^+}} = \frac{N_N}{N_O} = \frac{0.79}{0.21} \tag{16}$$

The conservation of charge:

$$p_{N^+} + p_{O^+} - p_{e^-} = 0 \tag{17}$$

and the summation of the mixture pressure:

$$\sum_s p_s = p_{mix} \tag{18}$$

With the above constraints, a nonlinear root finder can be used for solving the unknown partial pressure p_s for a given mixture pressure and temperature. In this project, the nonlinear root finder is implemented by the Newton method. The method uses the inverse of the constraint Jacobian to estimate the change of the partial pressure for each iteration. In addition to the classic Newton solver, this project uses normalized constraints to have better convergence at low temperatures and adds an if statement to ensure the partial pressures always stay positive during the iteration. The verifications of the eight-species model are shown in the section V.

E. Speed of Sound

The speed of sound is estimated from the isentropic compression/expansion of the air mixture:

$$a = \sqrt{\left(\frac{\partial p}{\partial \rho}\right)_s} \tag{19}$$

To obtain the relation between the pressure and density under the isentropic process, one may use the above constraints to formulate a relation between the partial pressure, density, and temperature:

$$\mathbf{J} d\vec{U} = [0, \ldots, dp, ds = 0]^T \tag{20}$$

where

$$\vec{U} = [\eta_{N_2}, \eta_{O_2}, \ldots, \eta_{e^-}, \rho, T]^T \tag{21}$$

and constraints Jacobian **J**:

$$\mathbf{J} = \begin{bmatrix} -\frac{\eta_N{}^2}{\eta_{N_2}{}^2} & 0 & 0 & \frac{2\eta_N}{\eta_{N_2}} & 0 & 0 & 0 & 0 & \frac{K_{p,1}}{\rho^2\hat{R}T} & \frac{K_{p,1}-TK'_{p,1}}{\rho\hat{R}T^2} \\ 0 & -\frac{\eta_O{}^2}{\eta_{O_2}{}^2} & 0 & 0 & \frac{2\eta_O}{\eta_{O_2}} & 0 & 0 & 0 & \frac{K_{p,2}}{\rho^2\hat{R}T} & \frac{K_{p,2}-TK'_{p,2}}{\rho\hat{R}T^2} \\ 0 & 0 & -\frac{\eta_N\eta_O}{\eta_{NO}{}^2} & \frac{\eta_O}{\eta_{NO}} & \frac{\eta_N}{\eta_{NO}} & 0 & 0 & 0 & \frac{K_{p,3}}{\rho^2\hat{R}T} & \frac{K_{p,3}-TK'_{p,3}}{\rho\hat{R}T^2} \\ 0 & 0 & 0 & -\frac{\eta_{N^+}\eta_{e^-}}{\eta_N{}^2} & 0 & \frac{\eta_{e^-}}{\eta_N} & 0 & \frac{\eta_{N^+}}{\eta_N} & \frac{K_{p,4}}{\rho^2\hat{R}T} & \frac{K_{p,4}-TK'_{p,4}}{\rho\hat{R}T^2} \\ 0 & 0 & 0 & 0 & -\frac{\eta_{O^+}\eta_{e^-}}{\eta_O{}^2} & 0 & \frac{\eta_{e^-}}{\eta_O} & \frac{\eta_{O^+}}{\eta_O} & \frac{K_{p,5}}{\rho^2\hat{R}T} & \frac{K_{p,5}-TK'_{p,5}}{\rho\hat{R}T^2} \\ \frac{2}{B} & -\frac{2A}{B^2} & \frac{B-A}{B^2} & \frac{1}{B} & -\frac{A}{B^2} & \frac{1}{B} & \frac{-A}{B^2} & 0 & 0 & 0 \\ 0 & 0 & 0 & 0 & 0 & 1 & 1 & -1 & 0 & 0 \\ \hat{M}_{N_2} & \cdots & \cdots & \cdots & \cdots & \cdots & \cdots & \hat{M}_{e^-} & 0 & 0 \\ \rho\hat{R}T & \cdots & \cdots & \cdots & \cdots & \cdots & \cdots & \rho\hat{R}T & (\sum_s \eta_s)\hat{R}T & (\sum_s \eta_s)\rho\hat{R} \\ \frac{\partial s_{mix}}{\partial \eta_{N_2}} & \cdots & \cdots & \cdots & \cdots & \cdots & \cdots & \frac{\partial s_{mix}}{\partial \eta_{e^-}} & \frac{\partial s_{mix}}{\partial \rho} & \frac{\partial s_{mix}}{\partial T} \end{bmatrix} \tag{22}$$

where

$$\begin{aligned} A &= 2\eta_{N_2} + \eta_{NO} + \eta_N + \eta_{N^+} \\ B &= 2\eta_{O_2} + \eta_{NO} + \eta_O + \eta_{O^+} \\ \frac{\partial s_{mix}}{\partial \eta_s} &= \frac{\partial s_s}{\partial \eta_s} = \hat{M}_s s_s - \hat{R} \\ \frac{\partial s_{mix}}{\partial \rho} &= \sum_s -\frac{\eta_s{}^2 \hat{R}^2 T}{p_s} \end{aligned} \tag{23}$$

Hence for any given pressure and temperature, the equilibrium states can be computed from the previous section. Then use the above relation to estimate $dp/d\rho$ with zero entropy change. With the pressure change ratio, the speed of sound can be obtained.

IV. Computational Fluid Dynamics

A. Governing Equations

The inviscid compressible flow can be considered as a system of nonlinear advection equations, for two-dimensional flow in Cartesian coordinates, which take the below form:

$$\frac{\partial \vec{U}}{\partial t} + \frac{\partial \vec{E}}{\partial x} + \frac{\partial \vec{F}}{\partial y} = 0 \tag{24}$$

The above vector form can be further described as follows and this equation set is known as the Euler equations:

$$\frac{\partial}{\partial t}\begin{bmatrix} \rho \\ \rho u \\ \rho v \\ E \end{bmatrix} + \frac{\partial}{\partial x}\begin{bmatrix} \rho u \\ \rho u^2 + p \\ \rho uv \\ (E+p)u \end{bmatrix} + \frac{\partial}{\partial y}\begin{bmatrix} \rho v \\ \rho uv \\ \rho v^2 + p \\ (E+p)v \end{bmatrix} = 0 \tag{25}$$

where the total energy per unit volume E is:

$$E = \rho e + \frac{1}{2}\rho\left(u^2 + v^2\right) \tag{26}$$

The Euler equations are derived from mass, momentum, and energy conservation. For this project, to simulate flow around a cylinder, coordinate transformation is applied to the nonlinear system equations. The coordinate transformation is expressed as follows:

$$\frac{\partial g\vec{U}}{\partial t} + \frac{\partial \vec{E}'}{\partial \xi} + \frac{\partial \vec{F}'}{\partial \eta} = 0 \tag{27}$$

where

$$\begin{bmatrix} \vec{E}' \\ \vec{F}' \end{bmatrix} = g \begin{bmatrix} \xi_x & \xi_y \\ \eta_x & \eta_y \end{bmatrix} \begin{bmatrix} \vec{E} \\ \vec{F} \end{bmatrix} \tag{28}$$

The spatial derivatives are based on the computational coordinate and the relation between the physical and computational domain is defined by the user. The remaining unknown part of the governing equation is the relation between conservative states $\vec{U}$ and the pressure and temperature. For the calorically perfect gas model, the pressure and the temperature can be explicitly evaluated as follows:

$$\begin{aligned} p &= \rho R_0 T \\ T &= \frac{\gamma_0 - 1}{R_0} e \end{aligned} \tag{29}$$

and the gas constant for the mixture, R_0, and heat capacity ratio, γ_0, for the ideal gas in this study are:

$$R_0 = 287.05\ J/mole \cdot K, \quad \gamma_0 = 1.4 \tag{30}$$

However, for the real gas model, the pressure and temperature become implicit:

$$\begin{aligned} p &= p(\rho, e) \\ T &= T(\rho, e) \end{aligned} \tag{31}$$

Therefore, a nonlinear root finder is also required for the computation to find the pressure and temperature with a given density and mixture of internal energy.

B. Constraints for the Real Gas Model

The gas composition can be solved similarly from the previous section. For convenience, the constraints here are based on the mole number per unit mass instead of partial pressure. This convention can directly introduce density into the equations without requiring an additional constraint. With given ρ and e, the nine constraints solve the composition of the eight species and temperature:
The dissociation of $N_2 \leftrightarrow 2N$:

$$\frac{(\eta_N)^2}{\eta_{N_2}} = \frac{K_{p,1}(T)}{\rho \hat{R} T} \tag{32}$$

The dissociation of $O_2 \leftrightarrow 2O$:

$$\frac{(\eta_O)^2}{\eta_{O_2}} = \frac{K_{p,2}(T)}{\rho \hat{R} T} \tag{33}$$

The dissociation of $NO \leftrightarrow N + O$:

$$\frac{\eta_N \eta_O}{\eta_{NO}} = \frac{K_{p,3}(T)}{\rho \hat{R} T} \tag{34}$$

The ionization of $N \leftrightarrow N^+ + e^-$:

$$\frac{\eta_{N^+} \eta_{e^-}}{\eta_N} = \frac{K_{p,4}(T)}{\rho \hat{R} T} \tag{35}$$

The ionization of $O \leftrightarrow O^+ + e^-$:

$$\frac{\eta_{O^+} \eta_{O^-}}{\eta_O} = \frac{K_{p,5}(T)}{\rho \hat{R} T} \tag{36}$$

The conservation of atoms:

$$\frac{2\eta_{N_2} + \eta_{NO} + \eta_N + \eta_{N^+}}{2\eta_{O_2} + \eta_{NO} + \eta_O + \eta_{O^+}} = \frac{N_N}{N_O} = \frac{0.79}{0.21} \tag{37}$$

The conservation of charge:

$$\eta_{N^+} + \eta_{O^+} - \eta_{e^-} = 0 \tag{38}$$

The summation of mass fraction is unity:

$$\sum_s \hat{M}_s \eta_s = 1 \tag{39}$$

and the conservation of the internal energy:

$$e_{mix} = \sum c_s e^s_{total}(T) \tag{40}$$

After solving the above constraints with the Newton solver for temperature and species composition, the pressure can be obtained:

$$p_{mix} = (\sum_s \eta_s)\rho \hat{R} T \tag{41}$$

C. Numerical Scheme

The CFD simulation of the hypersonic flow is based on computing the time evaluation of the conservative states in the flow field. In this project, the states are estimated in the computational domain and integrated via the first-order forward Euler method with the Courant–Friedrichs–Lewy number around 0.4:

$$\frac{\partial \vec{U}}{\partial t} = -\frac{1}{g}\left[\frac{\partial \vec{E}'}{\partial \xi} + \frac{\partial \vec{F}'}{\partial \eta}\right] \tag{42}$$

After obtaining the state fluxes based on the gas model, the remaining part is evaluating the spatial derivatives of the fluxes. The spatial derivatives are estimated by the finite difference method:

$$\left.\frac{\partial u}{\partial x}\right|_{x=x_i} \approx D_x u_i = \frac{1}{h}\sum_{l=-L_1}^{L_2} a_l u_{i+l} \tag{43}$$

For computing the value of the finite difference coefficients, this project uses the framework provided by Zhong [2] with three-point stencil and upwind parameter $\alpha = 1$ for stable first-order derivative estimation. To address the advective Riemann problem in supersonic flow, local Lax-Friedrich flux splitting is used to ensure the eigenvalues of the system remain positive or negative for upwind and downwind discretization:

$$\begin{aligned} \hat{E}^{\pm}_{LF} &= \frac{1}{2}\left[\vec{E}' \pm \lambda_E \vec{U}\right] \\ \hat{F}^{\pm}_{LF} &= \frac{1}{2}\left[\vec{F}' \pm \lambda_F \vec{U}\right] \end{aligned} \tag{44}$$

The maximum system eigenvalues are estimated as,

$$\begin{aligned} \lambda_E &= \sqrt{u'^2 + (\epsilon c)^2} \\ \lambda_F &= \sqrt{v'^2 + (\epsilon c)^2} \end{aligned} \tag{45}$$

where u' and v' are the maximum eigenvalue of the flux Jacobian and ϵ is a dissipation parameter, is set to 0.5, for smoothing the eigenvalue change and suppressing the carbuncle effect at the stagnation line [3].

D. Boundary Conditions

The boundary condition is given as follows. For the inflow condition, a supersonic inflow is used which is implemented with the Dirichlet boundary condition of the free stream states:

$$\vec{U}_{in} = \vec{U}_{free} \tag{46}$$

The outflow is computed simply through the time evolution of the states from the governing equation:

$$\frac{\partial \vec{U}_{out}}{\partial t} = -\left[\frac{\partial \vec{E}}{\partial x} + \frac{\partial \vec{F}}{\partial y}\right]_{out} \tag{47}$$

This implementation is feasible in this case due to the relatively high Mach number at the outlet and the solver is using a highly dissipative first-order upwind scheme. For the inviscid wall, the flow is impenetrable to the wall, the adiabatic condition is considered, and the pressure is computed with the momentum equation in radial direction:

$$\begin{aligned} \frac{\partial p_{wall}}{\partial r} &= \frac{\rho {u_\theta}^2}{r} \\ \frac{\partial u_\theta}{\partial t} &= -\frac{1}{r}\left(u_\theta \frac{\partial u_\theta}{\partial \theta} + \frac{1}{\rho}\frac{\partial p}{\partial \theta}\right) \\ u_r &= 0 \\ \frac{\partial T}{\partial r} &= 0 \end{aligned} \tag{48}$$

With all the boundary conditions given, the solver can start to simulate the fluid flow with appropriate initial values.

E. Interpolation Table

Since the Newton root finder for solving the constraints of ρ and e is relatively unstable compared with the p-T solver, this project uses an interpolation table to estimate the initial values of the real gas simulation from ideal gas CFD results. The table is pre-computed before the CFD simulation and the database covers the possible range of ρ and e for up to the hypersonic flow. The temperature range for the database is from 290K to 16, 000K and pressure ranges from 10^{-4} to 100 atm. After the values are obtained from the p and T solver, the interpolation table is built based on ρ and e are the x and y axis. The unstructured scatter data interpolation is realized by the Delaunay triangulation and interpolated linearly inside each Delaunay triangle. Most of the variables, such as ρ, e, and η, are saved in logarithmic space and temperature is the only variable saved linearly.

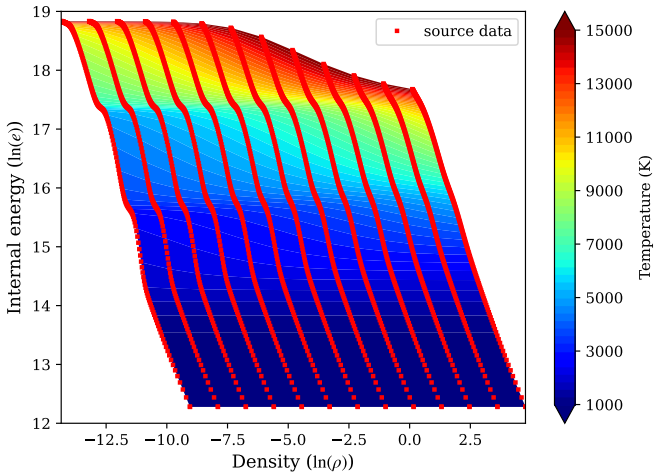

Fig. 1 The temperature map in the interpolation table for the initial guess of the gas composition

F. Simulation Workflow

The hypersonic flow simulation starts from the ideal gas model. The initial guess of the ideal gas is the free stream states. Due to the strong dissipative behavior of the first-order discretization, the ideal gas solution will eventually converge in a relatively short elapsed real-time compared with the real gas simulation. Then the density, ρ, and internal

energy, e, of the ideal gas solution will be used for computing the initial guess of the temperature, T, and gas composition, η, from the interpolation table. With the qualitatively correct initial guess, the ρ-e Newton solver can converge the pressure and temperature computation for each grid point. Then the CFD solver starts the time evolution simulation of the real gas hypersonic flow till the maximum percentage state changes over time is less than 0.01%. Worth noting, is the temperature contour of the initial guess from the interpolation table is slightly lower than the converged real gas solution. For the Mach 30 case, the stagnation temperature, from the initial guess to the converged solution, is increased from 9,315 K to 11,854 K which is about 27% change in temperature. This shows the necessity of performing a complete CFD simulation for the real gas model instead of just simply applying the real gas model to the converged ideal gas data. Figure 2 shows the workflow of the simulation procedure in order.

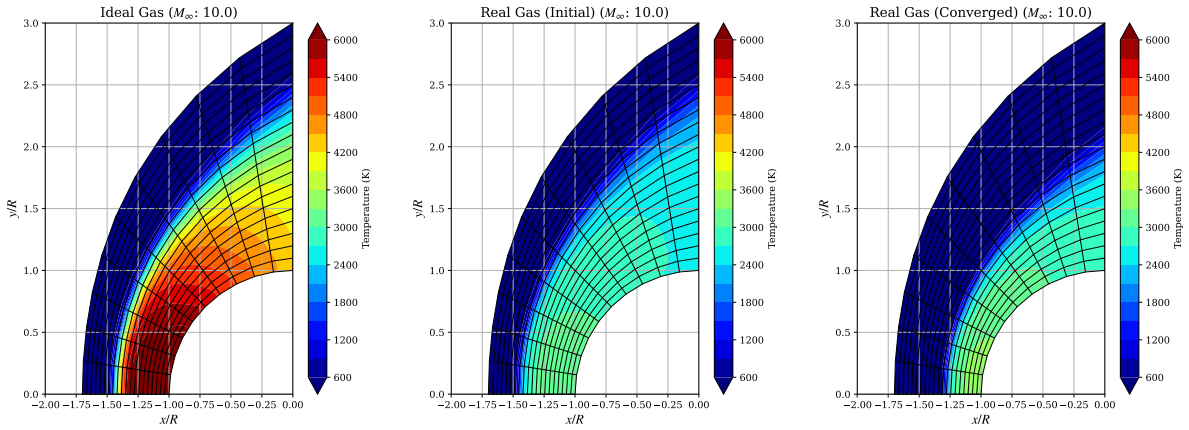

Fig. 2 The simulation workflow for the real gas simulation: the converged ideal gas solution (left), the initial guess of the real gas model based on the ideal gas solution (middle), and the converged real gas simulation (right)

V. Real Gas Model Verification

A. Comparison with the Literature

The eight-species equilibrium real gas model is verified by the works from Hansens [4, 5] and Hansens and Heims[6]. The first verified case is the compressibility of the mixture gas at the equilibrium state. The compressibility is computed as follows:

$$Z = \frac{\hat{M}_0}{\hat{M}} = (\sum_s \eta_s)\hat{M}_0 \tag{49}$$

Figure 3 shows the computed results compared with the data from Hansens [4]. The computed results have a close fit to the data which can be considered the proposed model is a valid for estimating the thermodynamic properties at high-temperature theoretically. The figure also shows that lowering the atmospheric pressure assists molecular dissociation more at the same temperature. This also makes sense since lower pressure has less resistance to keep the molecules together. Figure 4 shows the normalized internal energy. The normalized internal energy peaks around 9,000 to 13,000 K based on the given atmospheric pressure. These temperatures are the conditions where the gas starts to ionize and the zero energy of the ionized species starts to contribute to the internal energy. For a higher temperature, the influence of the ionized zero energy becomes smaller due to the species is fully ionized and the fixed zero energy is divided more by the increasing temperature. Figure 6 shows the speed of sound results. The data is a little bit off compared with other plots, especially in higher temperatures. One of the reasons may due that the proposed model only uses two terms to approximate the degenerate energy level for the electronic mode. For Hansen [4], some of the species, like N^+ and O^+, use up to six terms to approximate the electronic mode at high temperatures. Also, the results of the speed of sound have some discrepancies between the data from Hansens [4] and Hansens [5]. Regardless of the quantitative difference in the speed of sound computations, both simulations captured the oscillatory behavior of the speed when temperature increased. As previously predicted, the species tends to dissociate at lower temperatures and

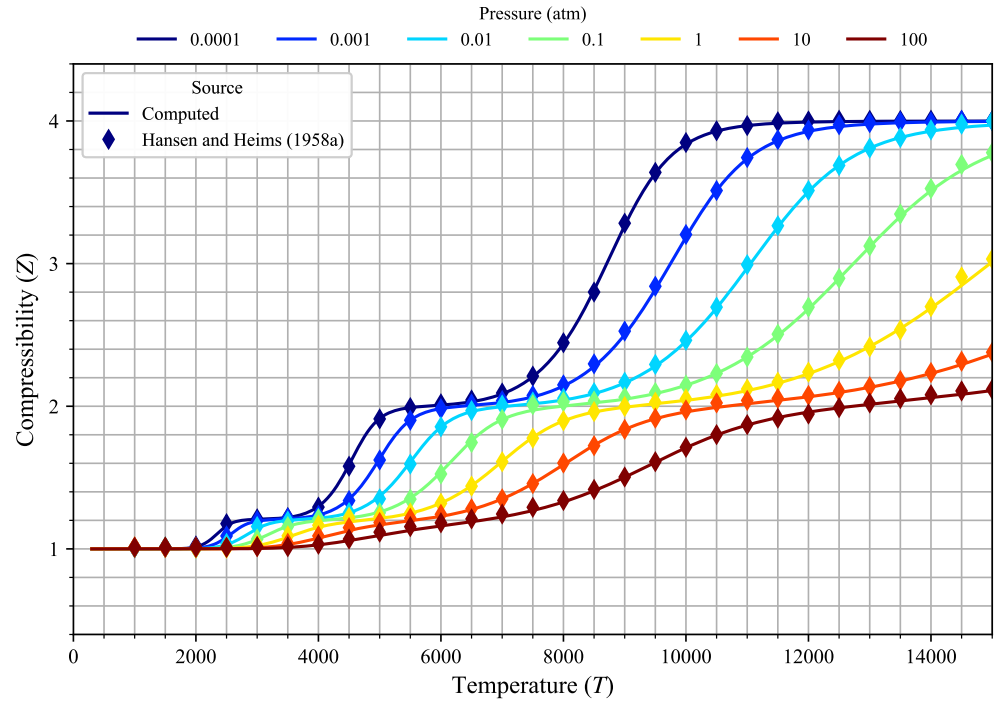

Fig. 3 The compressibility of the computed real gas model compared with the data from Hansens and Heims [4]

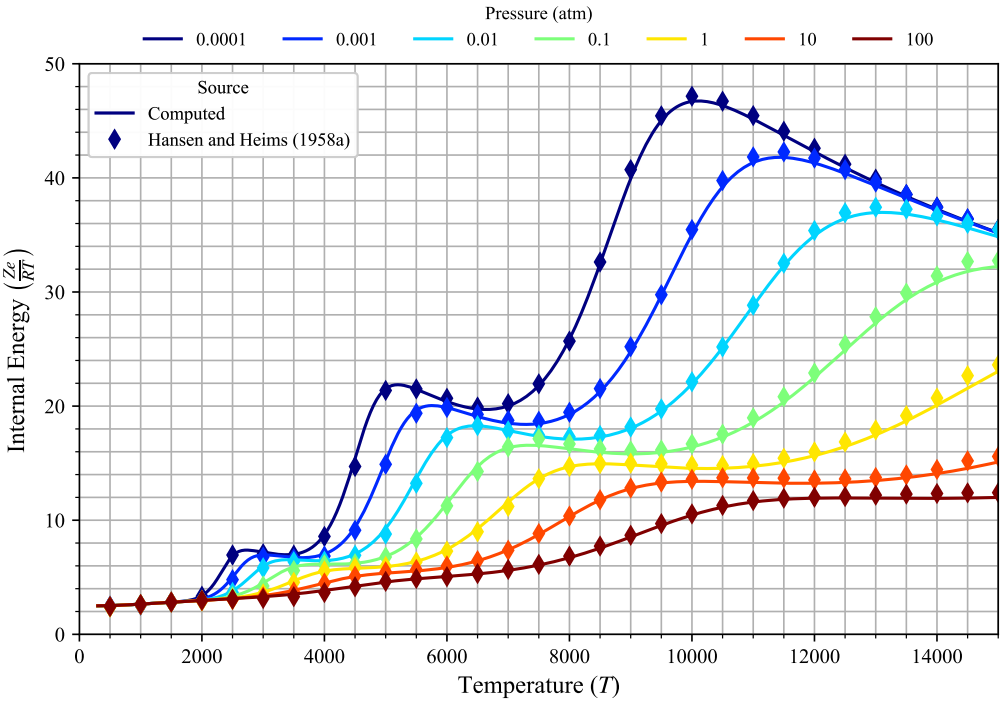

Fig. 4 The internal energy of the computed real gas model compared with the data from Hansens and Heims [4]

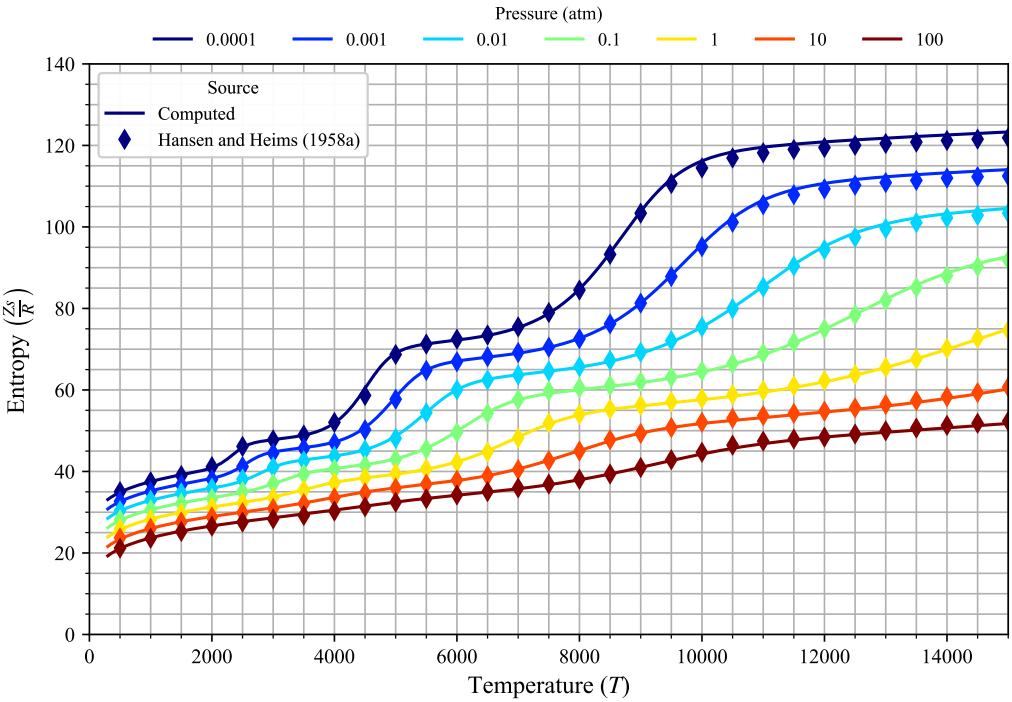

Fig. 5 The entropy of the computed real gas model compared with the data from Hansens and Heims [4]

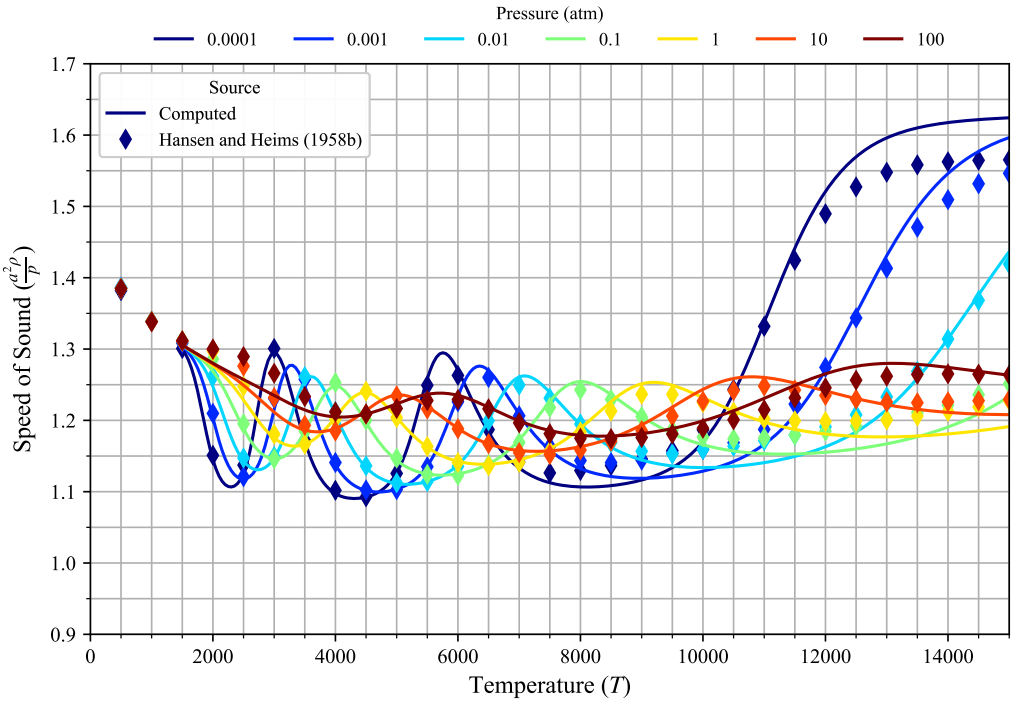

Fig. 6 The speed of sound of the computed real gas model compared with the data from Hansens and Heims [5]

B. Other Gas Properties

The rest of the plots are generated from the simulation without being directly verified by the literature. Figure 7 shows the simulated results for the normalized enthalpy and normalized density. The enthalpy has a similar trend as the internal energy. The peaks of the enthalpy curves happen when a species is dissociated or ionized. On the other hand, the density is the inverse of the compressibility. This is because the mixture becomes hard to compress with more dissociated molecules. Figure 8 and 9 are the species mass fraction under different temperatures. As previously predicted, the molecules are harder to dissociate under higher pressure. These plots can also serve as references for lookup

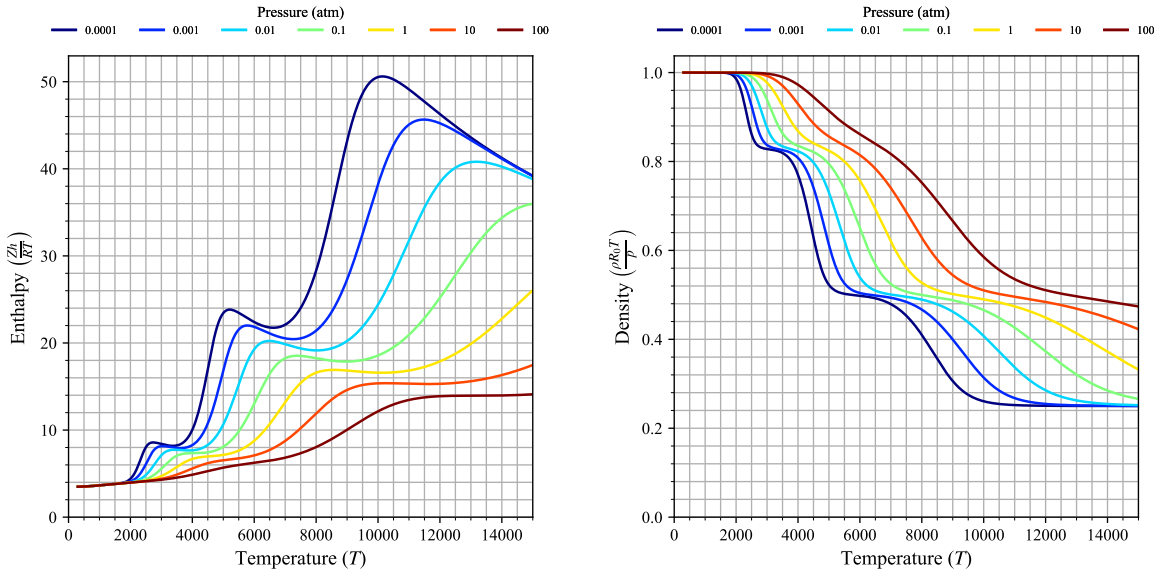

Fig. 7 The normalized enthalpy and density of the computed real gas model

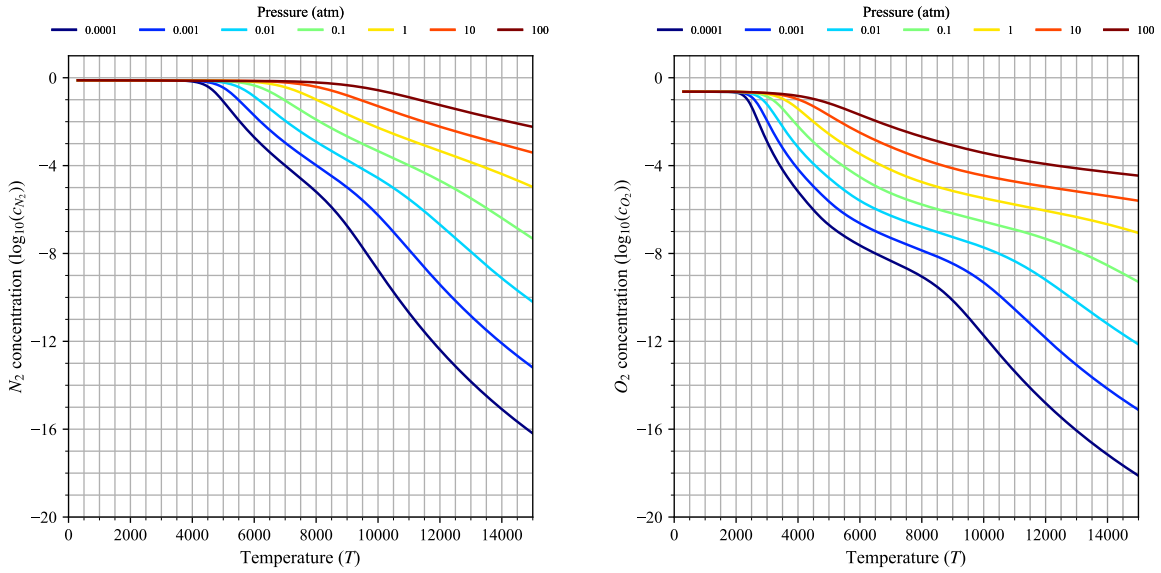

Fig. 8 The computed mass fraction of N_2 and O_2

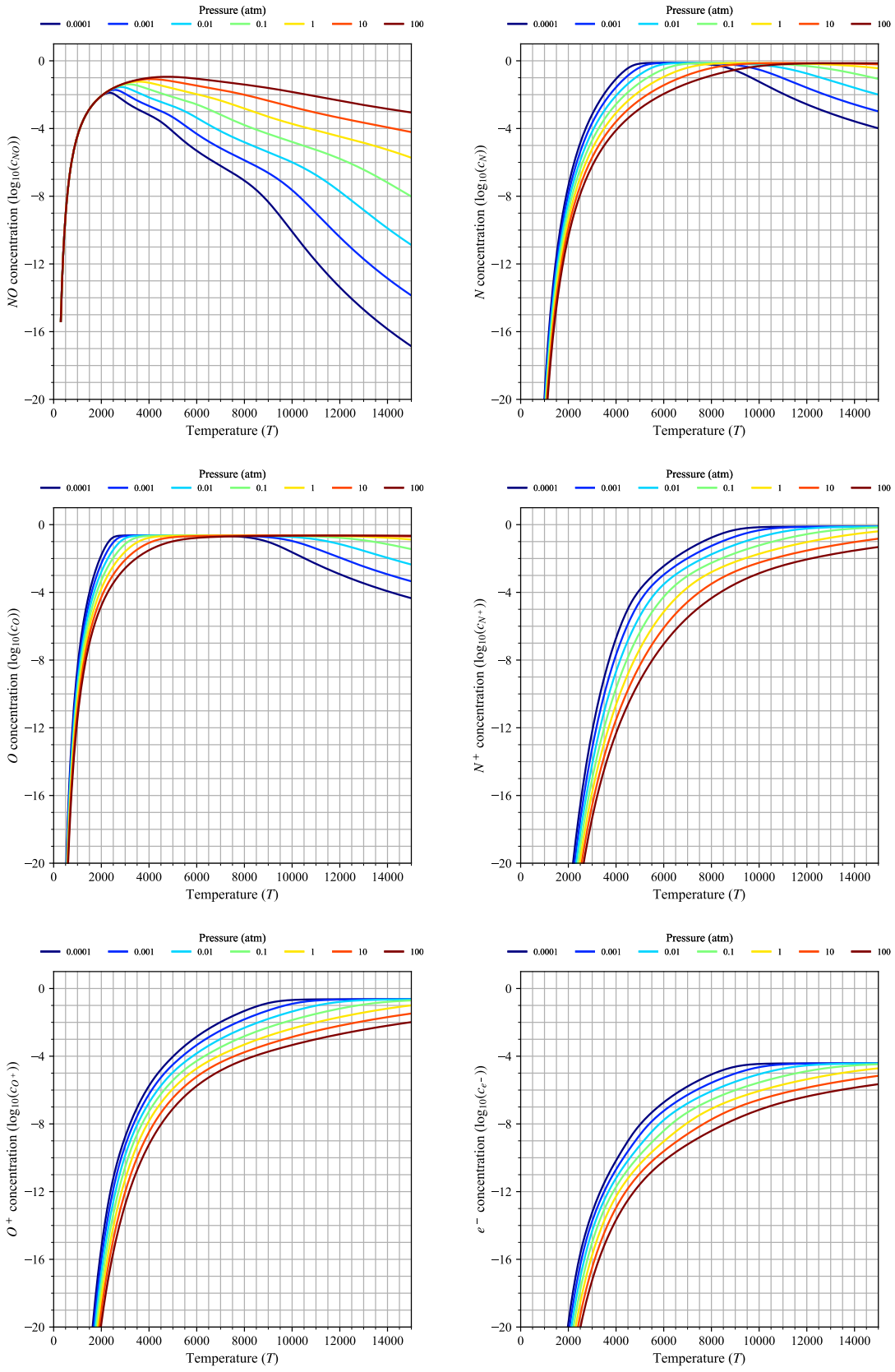

Fig. 9 The computed mass fraction of NO, N, O, N^{+}, O^{+} and e^{-}

VI. Hypersonic Flow over a Cylinder

The freestream conditions for the hypersonic simulations are pressure at 0.001 atm and temperature at 300 K. Figure 10-13 are the temperature contours from Mach 3 to 30. For lower Mach numbers, the real gas flow field is almost the same as the ideal gas. As the Mach number increases, the bow shock in the real gas model moves toward the cylinder faster than the ideal gas model which yields a thinner shock layer. The narrower shock layer is also a known property of the real gas model [7]. Figure 14 is the temperature comparison between the Anderson results for the temperature at the shock layer [7] and the computed maximum temperature in the flow field. The plot shows that the computed results are very close to the reference which can consider the model valid.

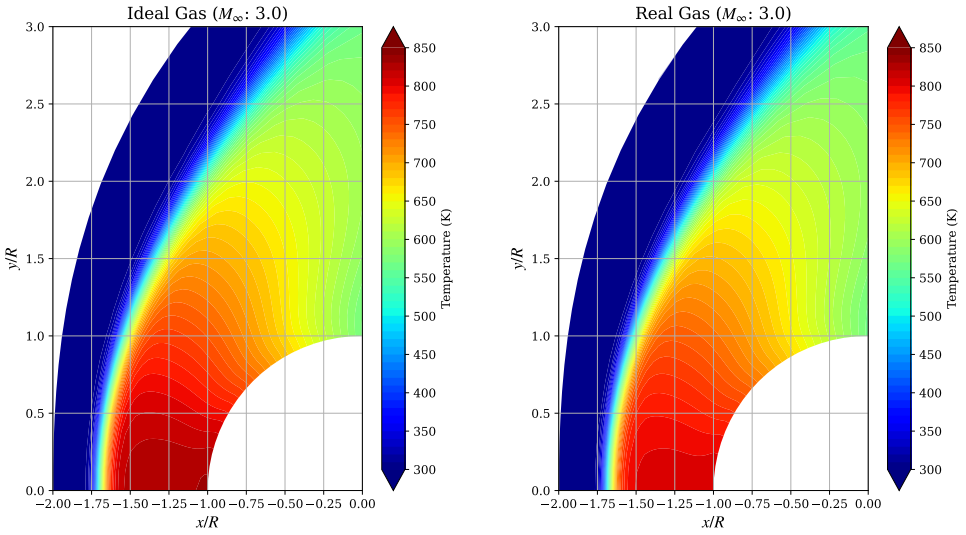

Fig. 10 The temperature contours for the Mach 3 case with the ideal gas model (left) and the real gas model (right)

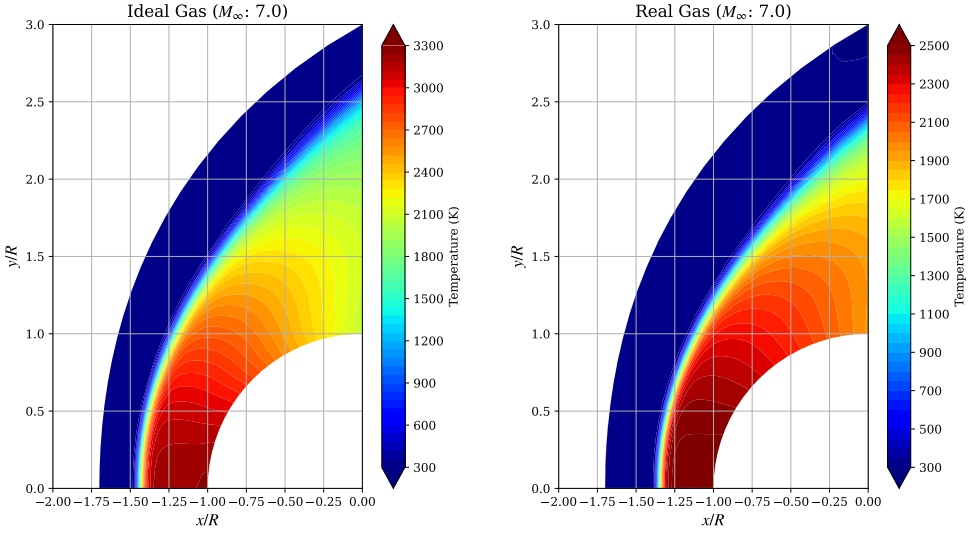

Fig. 11 The temperature contours for the Mach 7 case with the ideal gas model (left) and the real gas model (right)

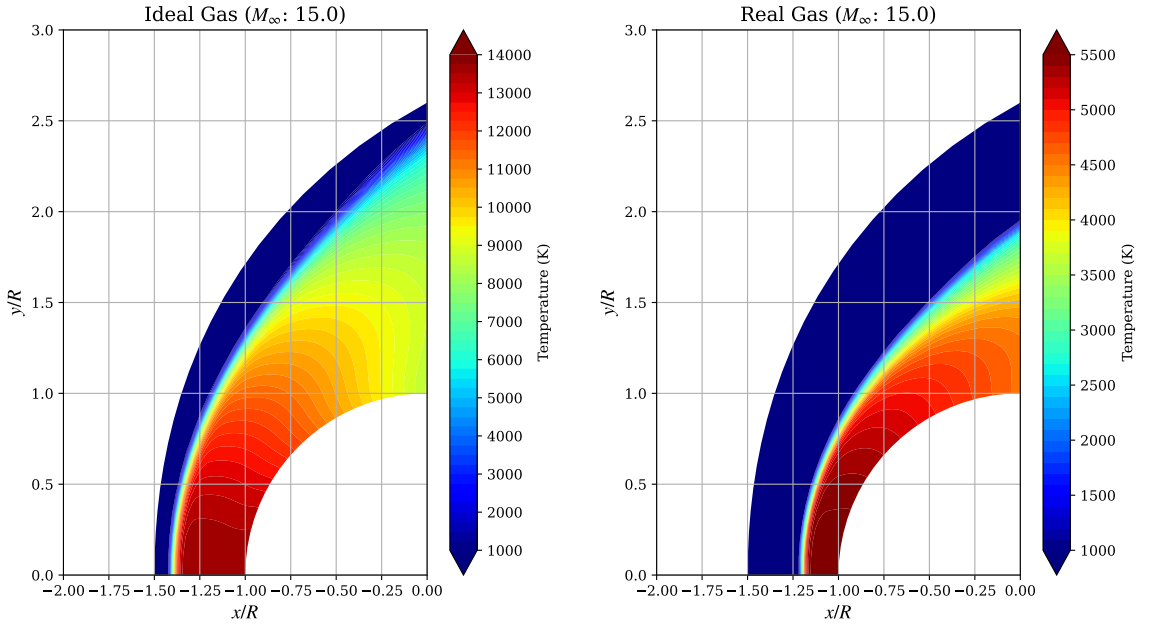

Fig. 12 The temperature contours for the Mach 15 case with the ideal gas model (left) and the real gas model (right)

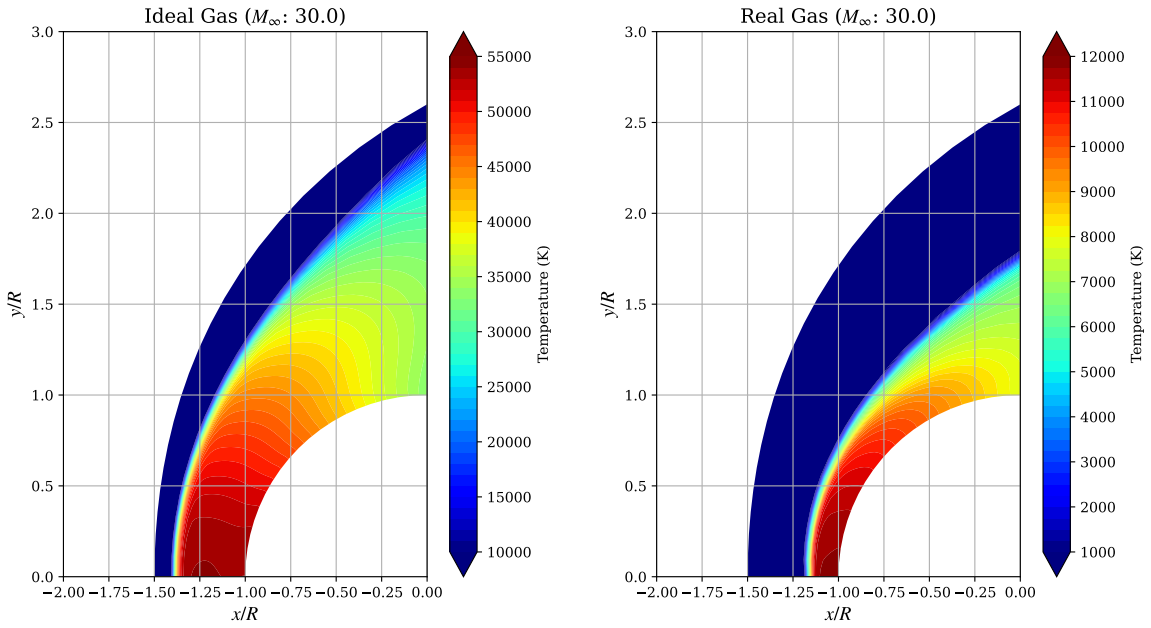

Fig. 13 The temperature contours for the Mach 30 case with the ideal gas model (left) and the real gas model (right)

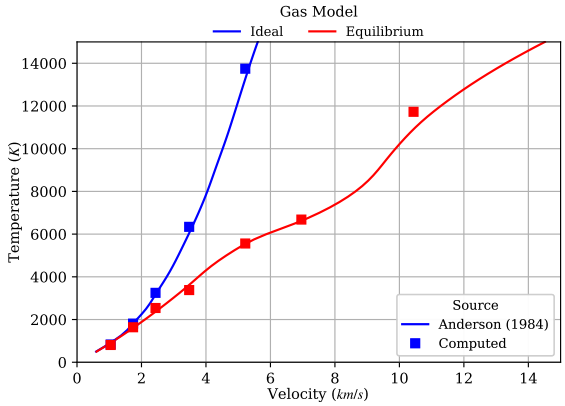

Fig. 14 The maximum temperature comparison of the hypersonic flow over a blunt body between the estimation from Anderson [7] and the computed results

VII. Discussions and Conclusions

This research project has demonstrated the capability of the numerical method on hypersonic flow simulations. In the real gas model computation section, the proposed eight-species equilibrium model reproduces the numerical data from Hansens [4, 5] and Hansens and Heims[6]. The compressibility, internal energy, and entropy of the air mixture closely fit with the data from the literature. Even though the speed of sound computation mismatches with the literature at higher temperatures, the overall results are still qualitatively consistent. One of the possible causes for this issue may be the proposed model's only the first two terms of degenerate energy level for the electronic mode. In contrast, the model from Hansens used up to six terms for the modes. The difference in the number of terms used will become distinct when the temperature rises. Hence increasing the number of terms used in the electronic mode can be one of the improvements for the proposed model.

In the CFD simulation section, the proposed method captures the critical difference between the ideal gas model and the real gas model. The simulated temperature of the proposed model is consistent with the data from Anderson [7] and reproduces the known real gas flow characters that have a thinner shock layer. However, due to the current program structure, the real gas simulation takes over a hundred times longer compared with the ideal gas simulation. Possible improvements are using a compiled language to make the code compute more efficiently, designing a specialized ρ-e solver for estimating pressure and temperature near the converged solution, and using a higher-order method with shock-fitting to reduce the number of grid points required.

References

[1] Sayler, K. M., and Service, C. R., "Hypersonic Weapons: Background and Issues for Congress," 2022.

[2] Zhong, X., "High-order finite-difference schemes for numerical simulation of hypersonic boundary-layer transition," *Journal of Computational Physics*, Vol. 144, No. 2, 1998, pp. 662–709.

[3] Phongthanapanich, S., "Healing of the carbuncle phenomenon for AUSMDV scheme on triangular grids," *International Journal of Nonlinear Sciences and Numerical Simulation*, Vol. 17, No. 1, 2016, pp. 15–28.

[4] Hansen, C. F., *Approximations for the thermodynamic and transport properties of high-temperature air*, 4150, National Advisory Committee for Aeronautics, 1958a.

[5] Hansen, C., "APPROXIMATIONS FOR THE THERMODYNAMIC AND TRANSPORT PROPERTIES OF HIGH-TEMPERATURE AIR," Tech. rep., National Aeronautics and Space Administration. Ames Research Center, Moffett . . . , 1959b.

[6] Hansen, C. F., and Heims, S. P., "A review of the thermodynamic, transport, and chemical reaction rate properties of high-temperature air," 1958.

[7] Anderson, J. D., *Hypersonic and high temperature gas dynamics*, AIAA, 1989.